

Lattice dynamics of β -FeSi₂ nanorods

J. Kalt,¹ M. Sternik,² I. Sergeev,³ M. Mikolasek,⁴ D. Bessas,⁴ J. Göttlicher,¹ B. Krause,¹ T. Vitova,⁵ R. Steininger,¹ O. Sikora,⁶ P. T. Jochym,² O. Leupold,³ H.-C. Wille,³ A. I. Chumakov,⁴ P. Piekarczyk,² K. Parlinski,² T. Baumbach,^{1,7} and S. Stankov^{1,7,*}

¹*Institute for Photon Science and Synchrotron Radiation, Karlsruhe Institute of Technology, D-76344 Eggenstein-Leopoldshafen, Germany*

²*Institute of Nuclear Physics, Polish Academy of Sciences, PL-31342 Kraków, Poland*

³*Deutsches Elektronen-Synchrotron, D-22607 Hamburg, Germany*

⁴*ESRF - The European Synchrotron, 71 Avenue des Martyrs, CS40220, 38043 Grenoble Cedex 9, France*

⁵*Institute for Nuclear Waste Disposal, Karlsruhe Institute of Technology, D-76344 Eggenstein-Leopoldshafen, Germany*

⁶*Faculty of Materials Engineering and Physics, Cracow University of Technology, PL-30084 Kraków, Poland*

⁷*Laboratory for Applications of Synchrotron Radiation, Karlsruhe Institute of Technology, D-76131 Karlsruhe, Germany*



(Received 15 July 2022; revised 20 October 2022; accepted 4 November 2022; published 17 November 2022)

Here we present a combined experimental and *ab initio* lattice dynamics study of the semiconducting β phase of FeSi₂. A polycrystalline β -FeSi₂ film was prepared on Si(111) and single-crystalline, self-assembled β -FeSi₂ nanorods were grown on Si(110) by molecular beam epitaxy. Both types of nanostructures were obtained by annealing of precursor structures, an epitaxial Fe film in the case of the film and high-aspect-ratio α -FeSi₂ nanowires in the case of the nanorods. The morphology and crystalline structure of the samples were investigated by reflection high-energy electron diffraction, atomic force microscopy, as well as x-ray diffraction and x-ray absorption spectroscopy. The Fe-partial phonon density of states (PDOS) was obtained from nuclear inelastic scattering. The PDOS of the film was investigated in the temperature range of 296 K down to 11 K and shows an excellent agreement with the *ab initio* calculations. In the PDOS of the nanorods, a shift in the number of states in the main features and an additional vibrational mode at 20 meV are observed. While the first effect can fully be explained by the specific orientation of the β -FeSi₂ unit cell on the Si(110) surface, the second effect is attributed to the formation of an α -FeSi₂ interlayer at the β -FeSi₂/Si interface. Furthermore, the thermoelastic properties of the film show a harmonic behavior in the investigated temperature range. For the nanorods, no significant deviation from the film is observed, except for a small decrease of the sound velocity.

DOI: [10.1103/PhysRevB.106.205411](https://doi.org/10.1103/PhysRevB.106.205411)

I. INTRODUCTION

Transition-metal silicides play a key role in the fabrication of present-day electronic devices due to their wide range of applications on the Si platform [1,2]. Among the large number of compounds included in this class of materials FeSi₂ is particularly interesting since it is the only representative that can be stabilized in both, metallic and semiconducting phases. The semiconducting equilibrium phase β -FeSi₂ has an orthorhombic unit cell (space group *Cmca*) with dimensions of $a = 9.86$ Å, $b = 7.79$ Å, and $c = 7.88$ Å [3]. It is stable up to 950 °C, above this temperature it transforms to the metallic α phase [4]. At room temperature β -FeSi₂ exhibits a direct band gap of 0.85 eV [5–9], which is equivalent to the absorption minimum of optical fiber at 1.5 μ m. At low temperatures, an indirect band gap with slightly lower energy was evidenced, together with an unusually large electron-phonon coupling coefficient [10]. Furthermore, β -FeSi₂ opens a possibility to fabricate integrated optoelectronic devices on the Si platform, which is not possible for pure Si with an indirect band gap. This promotes the use of β -FeSi₂ for

optoelectronic devices for information technology. Indeed, light-emitting diodes of Si/ β -FeSi₂ heterostructures have been realized by several groups [11–16]. In addition, its high thermal stability and large light absorption coefficient sparked the investigation of the application of β -FeSi₂ in photovoltaics [17–19].

Another field of interest is the use of β -FeSi₂ for thermoelectrics. Since it was first proposed for such applications in 1964 [20], a vast number of studies was published (e.g., Refs. [21,22]). The major advantages of β -FeSi₂ over most other thermoelectric materials are its availability, recyclability, and nontoxicity. Its possibilities as an environmentally friendly alternative have been impressively demonstrated by the production of β -FeSi₂ devices from cast iron scrap, reaching up to 90% of the figure of merit of devices made using pure Fe [23]. Promising approaches for the further improvement of the thermoelectric performance are doping [24–26] and reduction of the thermal conductivity by nanostructurization [27–29]. For instance, it was shown that the spatial confinement in β -FeSi₂ nanowires with diameters of about 100 nm has a significant impact on the thermal conductivity [30].

This wide range of applications initiated a thorough investigation of the growth of epitaxial thin films and nanoislands

*svetoslav.stankov@kit.edu

of β -FeSi₂ on Si substrates over the last decades. However, reports on the epitaxial growth of nanowires and nanorods remain scarce. Liang *et al.* reported the transformation of nanowires of an unknown Fe-Si phase into β -FeSi₂ nanowires upon annealing at 800 °C for 1h [31,32]. Furthermore, a study on the thermal stability of α -FeSi₂ nanowires revealed the transformation into β -FeSi₂ nanorods or three-dimensional islands by annealing at 800 °C for 1 h [33].

The lattice dynamics of bulk β -FeSi₂ has been studied theoretically [34,35] and by a combination of nuclear inelastic scattering (NIS) and *ab initio* calculations [36]. However, the technological application of this material in optoelectronics or thermoelectrics demands for an investigation of the effect of nanostructuring on the vibrational properties, since the lattice dynamics of nanostructures remarkably deviates from their bulk counterparts [37]. A large number of studies dedicated to this topic showed that one major origin of these deviations is the significant increase of the surface/interface-to-volume ratio due to the reduction of the dimensions to the nanometer length scale. This leads to a notable contribution of surface/interface-specific vibrational modes to the overall lattice dynamics, which manifest themselves in the emergence of additional states at low and high energies [38–42]. These alterations of the vibrational dynamics can influence the coupling of phonons with particles and quasiparticles, e.g., electrons [38,43], magnons [44], and other phonons [45]. Another potential source of anomalies is the formation of an interlayer between the nanostructures and the substrate, which can significantly influence the overall vibrational properties [46].

One major challenge in the experimental determination of the lattice dynamics of nanostructures is the inherently small scattering volume, which has to be accessed by inelastic scattering methods. Nuclear inelastic scattering [47,48] has proven to be uniquely suitable for such experiments. The technique, based on the Mössbauer effect, enables the determination of the phonon density of states (PDOS) of Mössbauer-active isotopes and thereby fundamental thermodynamic and elastic properties of crystals [49]. The resonant nature of the Mössbauer effect implies a large absorption cross section and provides an outstanding sensitivity down to a single atomic layer of material, while the high penetration depth of x-rays enables the measurement of buried layers and interfaces [39,50].

Here we present a combined NIS and *ab initio* study of the lattice dynamics of two types of β -FeSi₂ nanostructures. A polycrystalline β -FeSi₂ film is prepared by annealing of an epitaxial Fe film on a Si(111) substrate, whereas β -FeSi₂ nanorods are obtained by annealing of α -FeSi₂ nanowires on Si(110) substrates. A comprehensive structural characterization with various complementary techniques is performed. The PDOS of the film is in excellent agreement with the *ab initio* calculations and earlier publications. In comparison, the PDOS of the nanorods exhibit different intensities of the PDOS features, a damping of the spectral features and an additional peak at 20 meV. The experimental observations are explained by help of the *ab initio* calculations. Furthermore, the thermoelastic properties of the film are investigated as a function of temperature and compared to the results obtained for the nanorods.

II. EXPERIMENTAL AND THEORETICAL DETAILS

Two types of β -FeSi₂ nanostructures were grown under ultra high vacuum (UHV) conditions ($P < 1 \times 10^{-8}$ Pa). A β -FeSi₂ film was grown on the Si(111) surface, β -FeSi₂ nanorods on the Si(110) surface. The substrates were degassed in UHV at 650 °C for 4 h, followed by the removal of the native SiO₂ layer by heating two times to 1250 °C for 30 seconds. The subsequent growth process consisted of two stages. In a first step, a certain amount θ_{Fe} of high purity iron, enriched to 96 % in the Mössbauer-active isotope ⁵⁷Fe, was deposited on the substrate surface at the growth temperature T_G . The Fe deposition rate was monitored by a quartz crystal balance with an accuracy of 10 % and is given in Å and monolayer (ML) units. The given θ_{Fe} in Å corresponds to the thickness of an imaginary continuous Fe layer on the Si surface, whereas 1 ML is defined as one Fe atom per 1×1 Si(111) or Si(110) surface mesh. In a second step, these precursor structures were transformed into β -FeSi₂ by annealing at the temperature T_A for the duration t_A . This process is known as solid phase epitaxy. It is commonly applied for the growth of bulk β -FeSi₂ layers on Si(111) (e.g., Refs. [51,52]) and has also been reported for the growth of β -FeSi₂ nanostructures on Si(110) [31,33]. Details of the growth and experimental conditions used for the investigated samples, hereafter referred to as S1–S4, are summarized in Table I. All measurements described in the following were conducted at room temperature. The crystal structure and morphology of the nanostructures were investigated with a reflection high-energy electron diffraction (RHEED) device installed at the growth chamber and noncontact atomic force microscopy (AFM), conducted in an Omicron Large Sample scanning probe microscope. Both devices are part of the same UHV cluster and the sample transfer and the measurements were done under UHV conditions. Samples S1, S3, and S4 were subsequently capped with 4 nm of amorphous Si deposited by RF magnetron sputtering at room tempera-

TABLE I. Overview of the investigated samples. θ_{Fe} stands for the deposited amount of ⁵⁷Fe, T_G for the growth temperature, T_A for the annealing temperature and t_A for the annealing time. The morphology of the nanostructures after the annealing is given together with the respective average width, height, and length. The last row denotes if the sample was capped with Si or measured *in situ* in the NIS experiment.

Sample	S1	S2	S3	S4
Substrate	Si(111)	Si(110)	Si(110)	Si(110)
θ_{Fe} (Å)	50(5)	1.7(2)	0.6(1)	1.7(2)
θ_{Fe} (ML)	130(13)	3.0(3)	1.1(1)	3.0(3)
T_G (°C)	100(10)	630(10)	600(10)	600(10)
T_A (°C)	700(10)	750(10)	750(10)	750(10)
t_A (min)	10	120	180	240
Morphology	film	nanorods	nanorods	nanorods
\bar{w} (nm)	-	46	40	52
\bar{h} (nm)	16.2	10	9.5	12
\bar{l} (nm)	-	117	129	162
NIS exp.	Si cap	<i>in situ</i>	Si cap	Si cap

ture. The sputter chamber [53] with a base pressure of $P = 1 \times 10^{-6}$ Pa is also connected to the UHV cluster. The flux of the sputter gas Ar was 0.8 sccm, corresponding to a pressure of 0.36 Pa.

The crystal structure of the film S1 was investigated by x-ray diffraction (XRD) using Cu K α radiation. The local crystal structure of S1, S3, and S4 was studied by Fe K-edge x-ray absorption spectroscopy (XAS) at the SUL-X beamline of the synchrotron radiation source KARA at KIT. After calibration with an α -Fe metal foil to the Fe K edge at 7112 eV, the fluorescence emission of the samples was recorded up to $k = 14 \text{ \AA}^{-1}$. A beam-to-sample-to-detector geometry of $45^\circ/45^\circ$ was applied, using a collimated x-ray beam with a size of about $0.8 \times 0.8 \text{ mm}^2$, or a focused x-ray beam with $0.35 \times 0.15 \text{ mm}^2$ ($h \times v$, FWHM) at the sample position. The extended x-ray absorption fine structure (EXAFS) spectra were processed with the ATHENA program included in the IFEFFIT package [54].

The Fe-partial PDOS was obtained [55] from NIS experiments performed at the Dynamics Beamline P01 [56] at PETRA III and the Nuclear Resonance Beamline ID18 [57] at the ESRF. At both beamlines the measurements were performed in grazing-incidence geometry with an incidence angle $< 0.2^\circ$ and an x-ray beam with dimensions of $1.5 \times 0.01 \text{ mm}^2$ ($h \times v$, FWHM). The energy dependence of the probability for nuclear inelastic absorption was measured by tuning the energy of the x-ray beam around the ^{57}Fe resonance at 14.413 keV with an energy resolution of 0.7 meV for S1, S3, and S4 (ID18) and 1.0 meV for S2 (P01). Sample S2 was transported to the beamline and measured under UHV condition ($P < 5 \times 10^{-7}$ Pa) in a dedicated chamber [58]. For S1 additionally low-temperature NIS experiments were performed at 11 and 120 K using a He bath cryostat.

The *ab initio* calculations presented in the following chapters were performed within the density functional theory (DFT) implemented in the VASP code [59,60], employing the generalized gradient approximation [61,62]. The interaction between ions and valence electrons was described using the projector augmented-wave method [63,64]. Two systems were considered: (i) a bulk β -FeSi₂ crystal with an $(a, b\sqrt{2}, c\sqrt{2})$ supercell and (ii) a β -FeSi₂(100) slab with a thickness of one lattice constant a and a rectangular base with sides that are equal to the crystal lattice constants b and c . A vacuum of 10 \AA was used to separate two surfaces. The symmetry of the slab can be fully exploited when the Cartesian coordinate system is transformed and a $(b, c, a+\text{vac})$ supercell is used. Finally, to keep a similar density of k points for integration over the reciprocal space, a k mesh of (2,2,2) and (4,4,2) points in the Monkhorst-Pack scheme [65] was used for the bulk and slab, respectively. In the case of the bulk β -FeSi₂ crystal, a full relaxation of the lattice constants and atomic positions was carried out. The obtained lattice constants were then used to build the slab and were kept fixed during the optimization of the slab atomic positions. The structures were relaxed using the conjugate gradient technique with the energy convergence criteria set at 10^{-7} eV and 10^{-5} eV for the electronic and ionic iterations, respectively. The phonon dispersion relations were calculated using the direct method incorporated into the PHONON program [66,67].

III. RESULTS AND DISCUSSION

A. Structural investigation

Figure 1 shows RHEED patterns of S1-S4 before growth, after deposition of ^{57}Fe at T_G , and after the annealing process. After removal of the native oxide layer, a 7×7 reconstructed Si(111) surface is observed for S1 [Fig. 1(a)]. The deposition of 50 \AA ^{57}Fe at $T_G = 100^\circ\text{C}$ [Fig. 1(e)] results in the characteristic diffraction pattern of a crystalline Fe(111) surface [68–70]. The semicircles occurring after 10 min annealing at $T_A = 700^\circ\text{C}$ [Fig. 1(i)] suggest the formation of a polycrystalline film, while the additionally observed faint streaks are very similar to the Si(111) surface reflections. For S2–S4 a 16×2 reconstructed Si(110) surface [71] is observed after removal of the native oxide layer [Figs. 1(b)–1(d)]. The images are taken along the Si[001] direction, i.e., perpendicular to the expected orientation of nanowires grown on the Si(110) surface [72,73]. After deposition of the respective amount θ_{Fe} of ^{57}Fe , the typical diffraction pattern of α -FeSi₂ nanowires grown on Si(110) occurs for all three samples [Figs. 1(f)–1(h)] [72]. Although bulk α -FeSi₂ is stable only above 950°C , it can be grown in metastable nanostructures on Si surfaces due to the low lattice mismatch of certain crystallographic planes of both components. The straight streaks with superimposed diffraction spots confirm the formation of epitaxial and uniaxially aligned nanowires [72]. The annealing of S2 results in a reduction of the streak intensity and the emergence of additional diffraction spots, some of them are marked with white arrows in Fig. 1(j). This could either indicate the emergence of another crystal structure on the surface, a change in the epitaxial relation between the Si(110) surface and the α -FeSi₂ crystal, or a different surface morphology after the annealing. The diffraction patterns of S3 and S4 after the annealing [Figs. 1(k) and 1(l)] exhibit features of the bare Si(110) surface and similar additional spots as observed for S2. This suggests the formation of well separated nanostructures of the same type as in the case of S2.

The XRD data of the thin film S1 after the annealing process (Fig. 2) shows the Si(111) and Si(222) substrate reflections together with various β -FeSi₂ reflections. Because of the very similar lattice parameters b and c of the orthorhombic β -FeSi₂ unit cell, the angular spacing between a reflection with Miller indices (hkl) cannot be resolved from a $(h\bar{l}k)$ reflection, i.e., the β -FeSi₂(220) reflection for instance occurs approximately at the same angle as the β -FeSi₂(202) reflection. The diffraction pattern confirms the formation of a polycrystalline film, in agreement with the RHEED results [Fig. 1(i)]. Furthermore, the comparison with previous XRD results for the growth of β -FeSi₂ on Si(111) [36,51,74] shows that the sample is textured with the (220)/(202) planes being the preferential orientation parallel to the Si(111) surface.

Using S1 as a β -FeSi₂ reference, the crystal structure of S3 and S4 was investigated by x-ray absorption spectroscopy. The corresponding EXAFS spectra and EXAFS Fourier transforms are presented in Fig. 3. The EXAFS spectra of S1, S3, and S4 [Figs. 3(b) and 3(c)] show a very good agreement of the periodicity of the oscillations. The EXAFS Fourier transforms of S3 and S4, plotted in Figs. 3(e) and 3(f), are compared with the results obtained for S1 and additionally to α -FeSi₂ nanowires. Since the interatomic distances for the

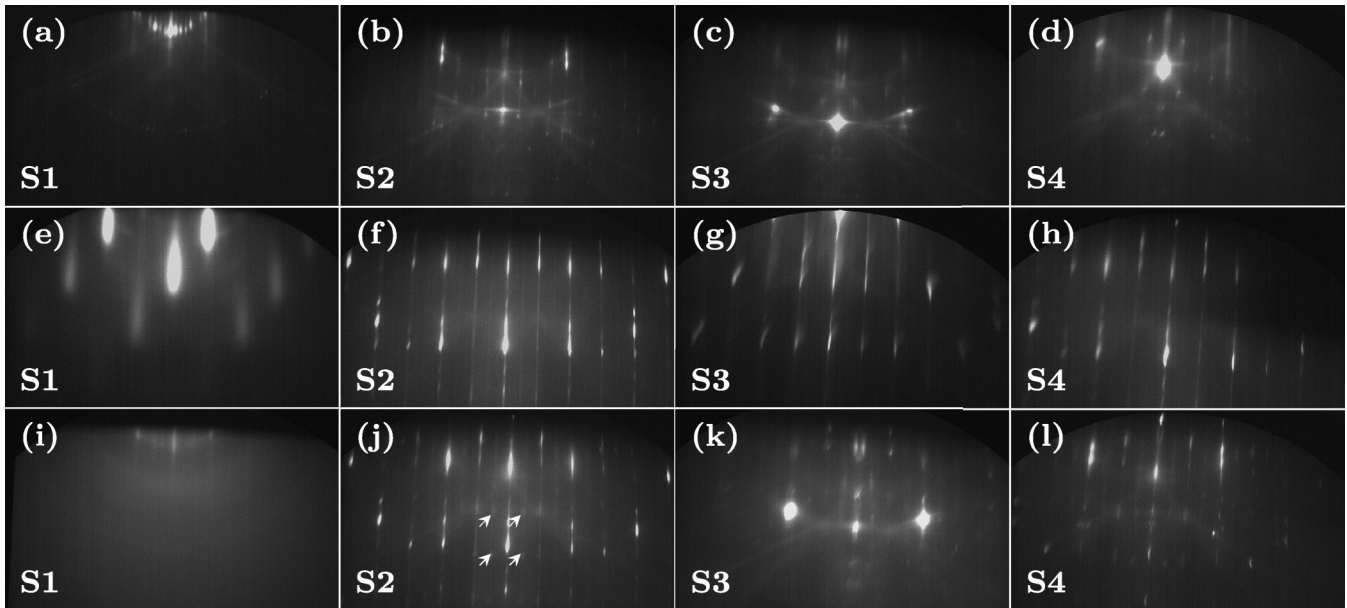


FIG. 1. RHEED patterns of the indicated samples obtained with a kinetic energy of $E = 28$ keV [(a)–(d)] before growth, [(e)–(h)] after ^{57}Fe deposition, and [(i)–(l)] after annealing. The images were taken along the $\text{Si}[\bar{1}10]$ direction of the $\text{Si}(111)$ surface for S1 and along the $\text{Si}[001]$ direction of the $\text{Si}(110)$ surface for S2–S4.

first coordination sphere, i.e., the Fe-Si scattering path, are the same for $\beta\text{-FeSi}_2$ and $\alpha\text{-FeSi}_2$, the corresponding peaks occur at the same radial distances. For the second coordination sphere, i.e., the Fe-Fe scattering path, $\beta\text{-FeSi}_2$ exhibits a larger interatomic distance than $\alpha\text{-FeSi}_2$ (compare ICSD 9119 and ICSD 5257). For S3 and S4, the peak of the second coordination sphere at around 2.7 Å is in good agreement with S1 and clearly deviates from the $\alpha\text{-FeSi}_2$ nanowires. Accordingly, the comparative XAS study confirms that the $\alpha\text{-FeSi}_2$ nanowires of S3 and S4 are mostly transformed into $\beta\text{-FeSi}_2$. However, the presence of small amount of other iron-silicide phases cannot be excluded by this approach.

Figures 4(a)–(d) show the AFM images obtained for S1–S4 after the annealing process, (e) shows an image of S2 after growth of the precursor $\alpha\text{-FeSi}_2$ nanowires. In (f), a generic line profile across a nanorod is presented, which was taken

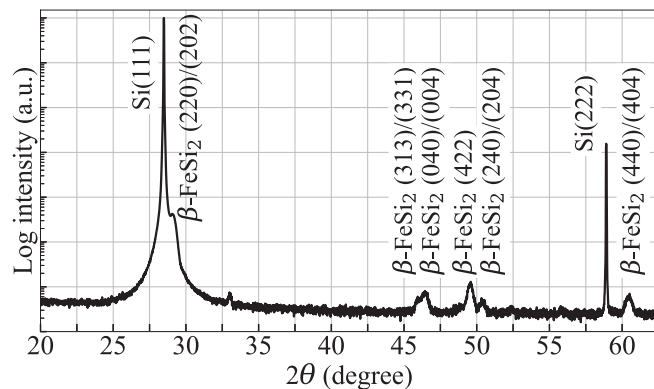


FIG. 2. X-ray diffraction data of S1 measured after annealing in θ - 2θ geometry with an x-ray energy of $E = 8.04$ keV. The peaks are labeled with the diffraction planes of the Si substrate and the $\beta\text{-FeSi}_2$ film.

along the white line shown in (c). In Table I, the average dimensions of the nanorods in Figs. 4(b)–(d) are given. For S1, the formation of an intermittent film is observed in Fig. 4(a). A film thickness 16.2 nm is measured as the step height between the uncovered areas of the $\text{Si}(111)$ surface and the film surface. The expected film thickness can be calculated from the number of deposited Fe atoms per unit area and the number of Fe atoms per $\beta\text{-FeSi}_2$ unit cell and amounts to 16.4 nm. For S2–S4, the annealing leads to the formation of short nanorods which are oriented along $\text{Si}[\bar{1}10]$. A comparison of Figs. 4(b) and 4(e) shows that after the annealing still traces of remnant $\alpha\text{-FeSi}_2$ nanowires are visible in the case of S2, whereas the longer annealing in the case of S3 and S4 leads to a complete transformation of the nanowires into nanorods. In combination with the EXAFS results, this confirms the phase sequence and the morphology evolution for the annealing of high-aspect-ratio FeSi_2 nanowires on $\text{Si}(110)$ reported in Ref. [33]. The morphology change during the transformation process occurs abruptly, i.e., high-aspect-ratio $\alpha\text{-FeSi}_2$ nanowires are directly transformed into compact $\beta\text{-FeSi}_2$ nanorods without undergoing a continuous morphology change. The absence of an intermediate step is probably connected to the large lattice mismatch between $\beta\text{-FeSi}_2$ and Si compared to the metastable $\alpha\text{-FeSi}_2$. As a consequence, a minimum volume-to-interface ratio is required to compensate the higher $\beta\text{-FeSi}_2/\text{Si}(110)$ interface energy induced by the epitaxial strain. For all three samples, the transformation from nanowires to nanorods is accompanied by the formation of a deep trench along the long side of the nanorods. Earlier publications reported a similar trough formation at the tip of CoSi_2 [75] and MnSi_2 [76] nanowires grown on $\text{Si}(110)$. It was attributed to the large Si supply required for the growth of the silicide nanostructures. The evaluation of AFM line profiles showed that the nanorods exhibit two distinct side facets. The angle between the Si surface and the facet facing

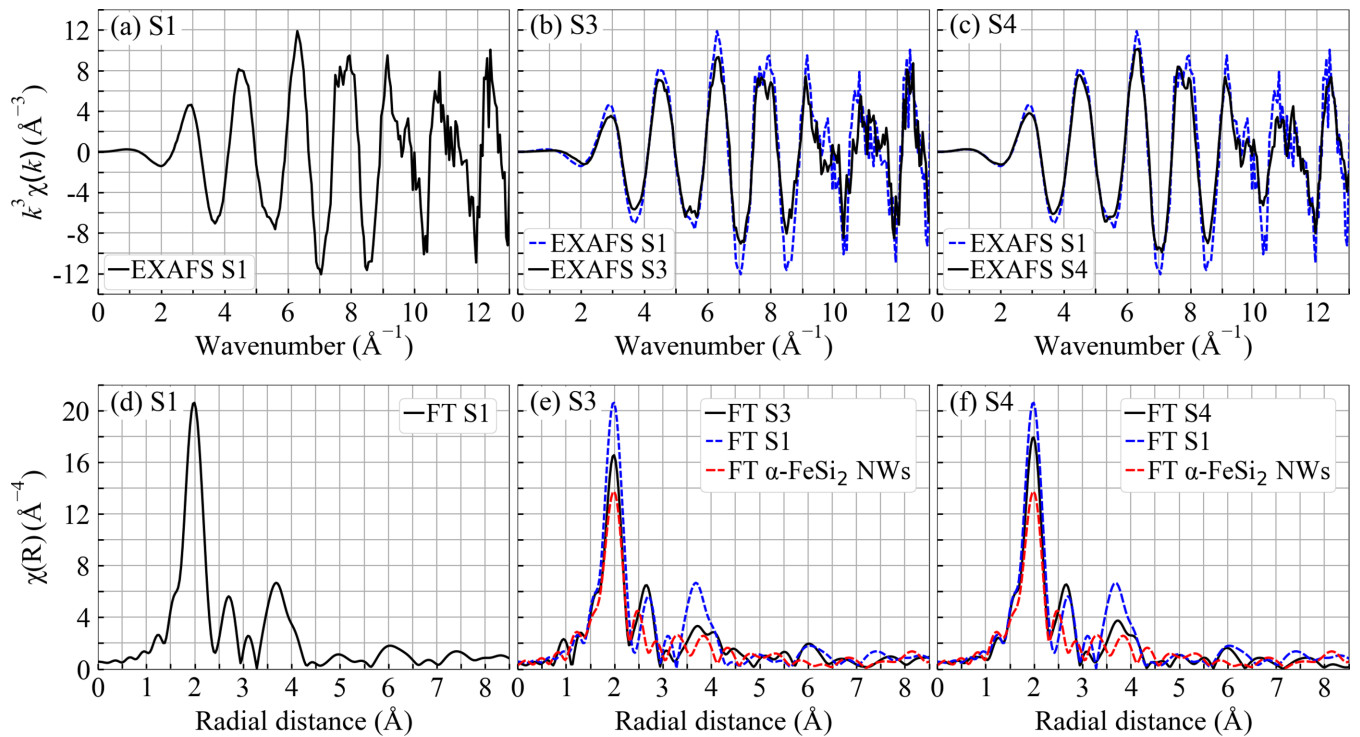


FIG. 3. [(a)–(c)] Fe K -edge EXAFS spectra of S1, S3, and S4. The spectra are weighted with k^3 for amplification of the oscillations at higher k values. [(d)–(f)] Fourier transforms (FT) of the EXAFS spectra shown above. Samples S3 and S4 are compared with an exemplary EXAFS FT curve of α -FeSi₂ nanowires (red dashed line) published elsewhere [72].

the trench amounts to $35.3^\circ \pm 2.3^\circ$ and the opposite facet to $16.7^\circ \pm 0.9^\circ$, where the error represents the standard deviation. Furthermore, the small pyramidal nanodots, which are scattered over the surface in the case of S2–S4, are already present after growth of the α -FeSi₂ nanowires [72,73].

B. Lattice dynamics

In Fig. 5, the *ab initio* calculated phonon dispersion relations (PDR) of bulk β -FeSi₂ and the β -FeSi₂(100) surface are depicted. The β -FeSi₂ primitive cell contains 24 atoms. The Fe and Si atoms occupy two nonequivalent sites each (4 Fe_I, 4 Fe_{II} and 8 Si_I, 8 Si_{II} atoms), leading to a rather complex PDR with a total of 72 branches for bulk β -FeSi₂ [35,77], as visible in Fig. 5(a). The results are in agreement with the previously reported PDR obtained from first-principles calculations for bulk β -FeSi₂ [35]. In Fig. 5(b), the number of dispersion curves increases to 156 as the slab supercell, which is identical with the slab primitive unit cell, contains a total of 52 atoms. Due to the reduced coordination of the surface atoms, many phonon branches are shifted to lower energies compared to their bulk counterparts.

In Fig. 6(a), the orientation of the β -FeSi₂ unit cell on the Si(110) surface is illustrated, together with the *ab initio* calculated Fe-partial PDOS of (b) bulk β -FeSi₂ and (c) the β -FeSi₂(100) surface slab. The total PDOS is decomposed into the contributions of x -, y -, and z -polarized phonons. The large number of vibrational modes leads to a broad frequency distribution of the normal modes in both cases. The Fe-partial PDOS of bulk β -FeSi₂ is characterized by a broad peak at 37 meV, a plateau between 24 and 30 meV, two minor peaks

at 44 and 48 meV, and a cutoff energy of 62 meV. The results are in good agreement with earlier *ab initio* calculations [36]. The direction-projected PDOS shows very similar spectra for phonons with polarization along the y and z directions, whereas x -polarized phonons exhibit a stronger contribution to the total PDOS between 20 and 30 meV and a lower contribution to the main peak around 37 meV. This shift to lower energies of the vibrations polarized along the x direction of the orthorhombic unit cell can be explained by the larger interatomic distances and the consequently reduced interatomic force constants compared to y and z directions. The overall PDOS of the β -FeSi₂(100) surface shows a strong shift to lower energies with pronounced peaks at 14, 17, and 21 meV and an extended tail with a cutoff energy at 57 meV. The PDOS of y - and z -polarized phonons exhibit several overlapping peaks between 12 and 18 meV, the PDOS of x -polarized phonons is mainly localized in two intense peaks at 18 and 21 meV.

The Fe-partial PDOS of the film S1, obtained along the orthogonal directions Si[$\bar{1}10$] and Si[$1\bar{1}2$] of the Si(111) surface, is shown in Fig. 7(a). Both spectra are almost identical and characterized by a pronounced peak at about 36 meV, minor peaks between 40–45 meV, a plateau between 24–28 meV and a cutoff energy of 60 meV. The isotropic vibrational behavior revealed by the spectra obtained along the orthogonal directions can be explained by the polycrystalline nature of the β -FeSi₂ film, evidenced by the RHEED and XRD studies. The variously oriented domains lead to averaged relative contributions of x -, y -, and z -polarized phonons of approximately 1/3 for both orientations of the x -ray beam with respect to the substrate. Compared to the *ab initio* calculated PDOS

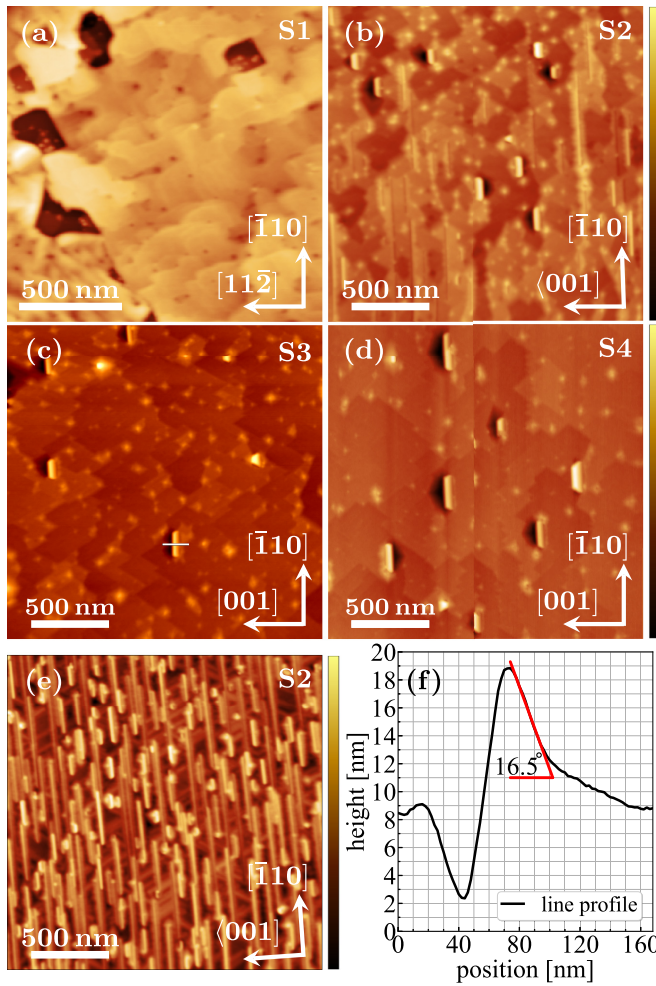


FIG. 4. AFM images of S1–S4 after annealing with height scale (a) 0–47, (b) 0–26, (c) 0–28, and (d) 0–29 nm. (e) shows S2 after growth of the α -FeSi₂ nanowires with height scale 0–13 nm. The crystallographic directions of the (a) Si(111) and [(b)–(e)] Si(110) surfaces are given with arrows. In (f), an exemplary line profile of a nanorod of S3, corresponding to the white line in (c), is presented.

the experimental data show a small shift to lower energies. A similar shift was observed for the PDOS of a polycrystalline β -FeSi₂ film grown on a Si(100) substrate [36] and attributed to either slightly smaller calculated lattice constants or anharmonic contributions. Therefore the energy scale of the *ab initio* PDOS, plotted with a red line in Fig. 7(a), is scaled by a factor of 0.97 for comparison. The *ab initio* PDOS is calculated from the energy dependence of the absorption probability density of β -FeSi₂, convoluted with a Voigt function with FWHM = 0.7 meV, which is equal to the experimental resolution. Including these corrections, only minor deviations are observed between the *ab initio* calculations and the experiment. In Fig. 7(b), the PDOS of S1 at 11, 120, and 296 K are compared. A significant temperature-dependence of the PDOS, e.g., induced by the previously reported strong electron-phonon-coupling [10] or anharmonic effects, is not observed. The main effect is a small shift to higher energies in the spectra measured at lower temperatures, which amounts to about 0.7 meV for the main peak of the PDOS measured at 11

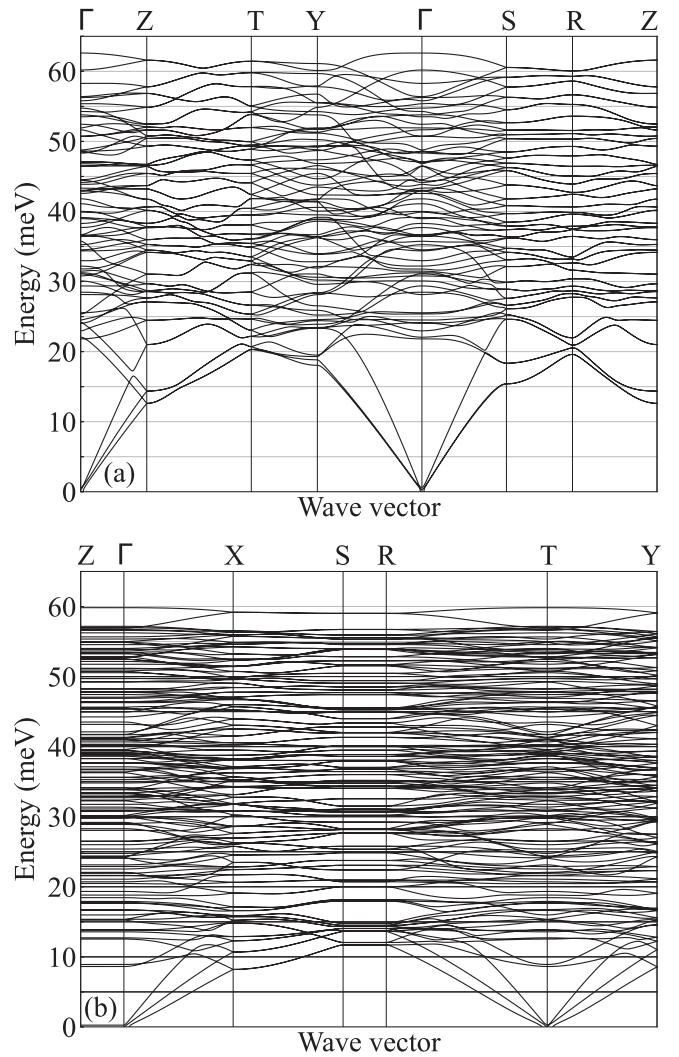


FIG. 5. *Ab initio* calculated phonon dispersion relation of (a) bulk β -FeSi₂ and (b) the β -FeSi₂ slab with (100) surface.

and 296 K. This shift occurs as a result of the reduced average interatomic distances at lower temperatures. In general, the small broadening of the measured PDOS, compared to the theoretical one, and rather minor dependence on temperature indicate weak anharmonic effects in the temperature range from 11 K to room temperature.

Figure 8 shows the Fe-partial PDOS of S2–S4 obtained with the x-ray wave vector oriented along the orthogonal Si(110) surface directions Si $\bar{1}10$ and Si 001 (see Fig. 4), respectively along and across the nanorod orientation. The main features of the spectra of the film S1 are also observed for the nanorods. However, a small decrease in the number of states in the plateau between 24–28 meV and a small increase in the minor peaks between 40–45 meV is observed. Furthermore, an additional peak at 20 meV appears. The intensity of the peak is increasing with increasing annealing duration from S2–S4 and the contribution to the overall PDOS is stronger in the spectra obtained across the nanorods.

The different intensity at 24–28 meV and 40–45 meV in the PDOS of S2–S4 compared to S1 can be explained by the unique orientation of the β -FeSi₂ crystal with respect

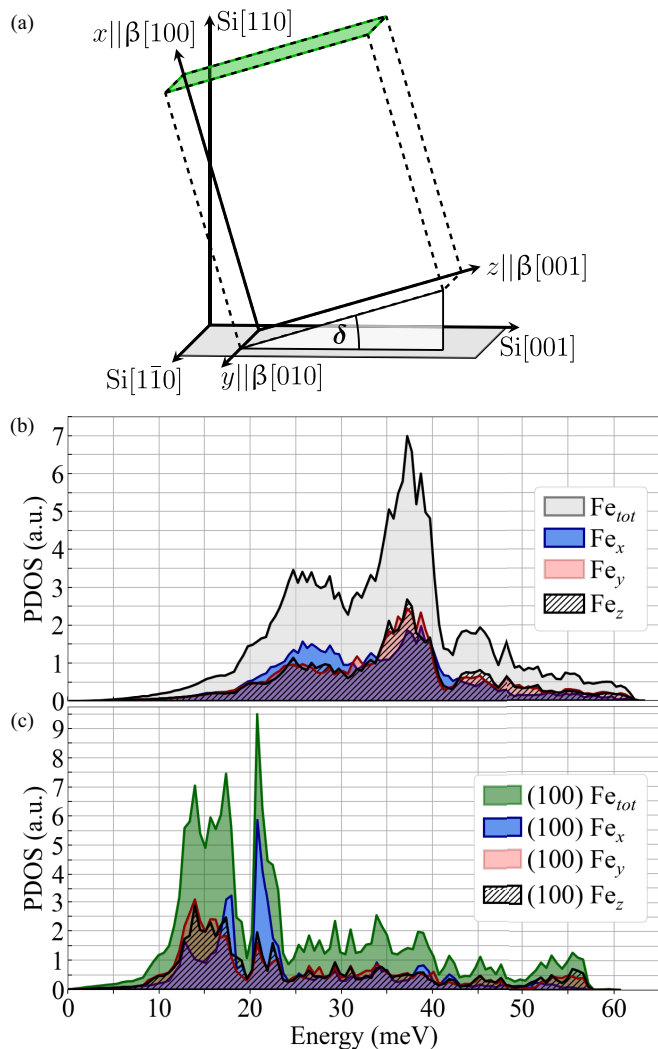


FIG. 6. (a) Sketch of the β -FeSi₂ unit cell on Si(110), following the epitaxial relation described in the text. The inclination angle between the Si(110) surface (gray shaded) and the β -FeSi₂(100) plane (green shaded) is given by δ . Below, total and direction-projected *ab initio* calculated Fe-partial PDOS (b) of bulk β -FeSi₂ and (c) of the β -FeSi₂ slab with (100) surface are depicted.

to the direction of the incoming x-ray beam in the case of the nanorods, which is not the case for the polycrystalline film. The RHEED images of Figs. 1(j)–(l) indicate that the β -FeSi₂ crystal of the nanorods exhibits one single domain orientation with a distinct epitaxial relation to the substrate. In a single-crystalline lattice with noncubic symmetry, the PDOS obtained with the x-ray wave vector being oriented along a certain crystallographic direction is composed of a specific combination of x -, y -, and z -polarized phonons [78,79]. The relative weight of each contribution, named A_x , A_y , and A_z in the following, along the specific measurement direction can be calculated by projection of the incoming x-ray beam along the main crystallographic directions. Prerequisite for this is the knowledge of the orientation of the β -FeSi₂ unit cell on the Si(110) surface.

The epitaxial growth of β -FeSi₂ on Si(111) and Si(001) substrates is well investigated (e.g., Refs. [3,13,80–83]). The

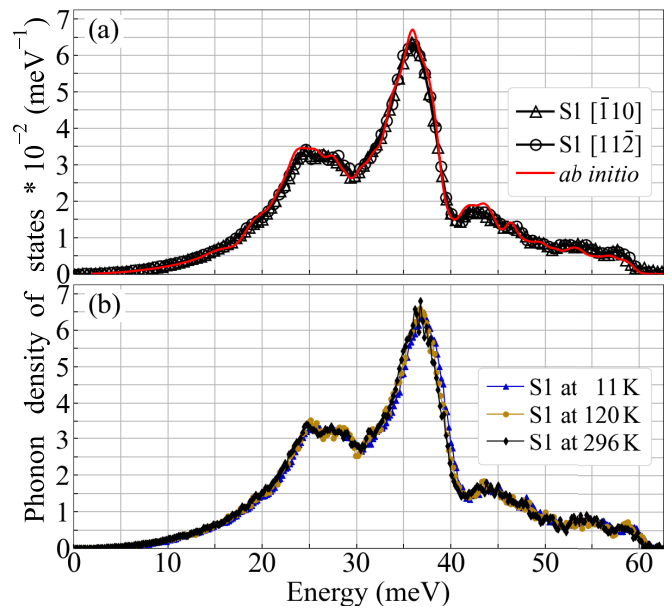


FIG. 7. (a) Fe-partial PDOS of S1 obtained at 296 K along the orthogonal surface directions Si[110] and Si[112]. The red solid line indicates the *ab initio* calculated PDOS of bulk β -FeSi₂, convoluted with a Voigt profile with FWHM=0.7 meV and scaled by a factor of 0.97 as described in the text. (b) Fe-partial PDOS of S1 obtained along Si[112] at the indicated temperatures.

small difference of 1.1% in the b and c lattice parameters of the orthorhombic unit cell allows two different accommodations of the β -FeSi₂ on the Si surface. The commonly reported epitaxial relations are (i) β -FeSi₂(101)||Si(111) with β -FeSi₂[010]||Si[110] and (ii) β -FeSi₂(110)||Si(111) with β -FeSi₂[001]||Si[110] (e.g., Refs. [3,81]). It was shown that both configurations coexist in the very same β -FeSi₂ film on Si(111) surfaces [80] with an estimated ratio (i)/(ii) of 45/55 [83]. In contrast, the reports on the epitaxial relation of β -FeSi₂ on Si(110) remain scarce. In Ref. [31], it is reported that the transformation of metastable FeSi₂ nanowires on Si(110) into β -FeSi₂ results in the formation of endotaxial nanowires with an epitaxial relation of β -FeSi₂(101)||Si(111) with β -FeSi₂[010]||Si[110] or β -FeSi₂(110)||Si(111) with β -FeSi₂[001]||Si[110] [31], which is equivalent to the above discussed case on Si(111). Endotaxy refers to the property of silicides to grow into the substrate, in order to form a coherent interface with a preferential Si lattice plane which is inclined with respect to the surface [84]. A RHEED study on the formation of Fe-Si compounds on Si(110) inferred that the epitaxial relation is given by (a) β -FeSi₂(410)||Si(110) with β -FeSi₂[001]||Si[110] or (b) β -FeSi₂(401)||Si(110) with β -FeSi₂[010]||Si[110] [85], which is equivalent to a rotation of the above discussed relation by only 1.3° around Si[110]. Translation of the epitaxial relation reported for β -FeSi₂ on Si(111) to the Si(110) surface results in an upright oriented β -FeSi₂ unit cell as depicted in Fig. 6(a). The inclination angle δ between Si[001] and β -FeSi₂[001] amounts to 16.1° for configuration (i) and 16.4° for configuration (ii). These calculated angles fit very well to the 16.7° ± 0.9° determined by AFM between the Si(110) surface and the surface facet of the nanorods opposite to the trench. This supports that

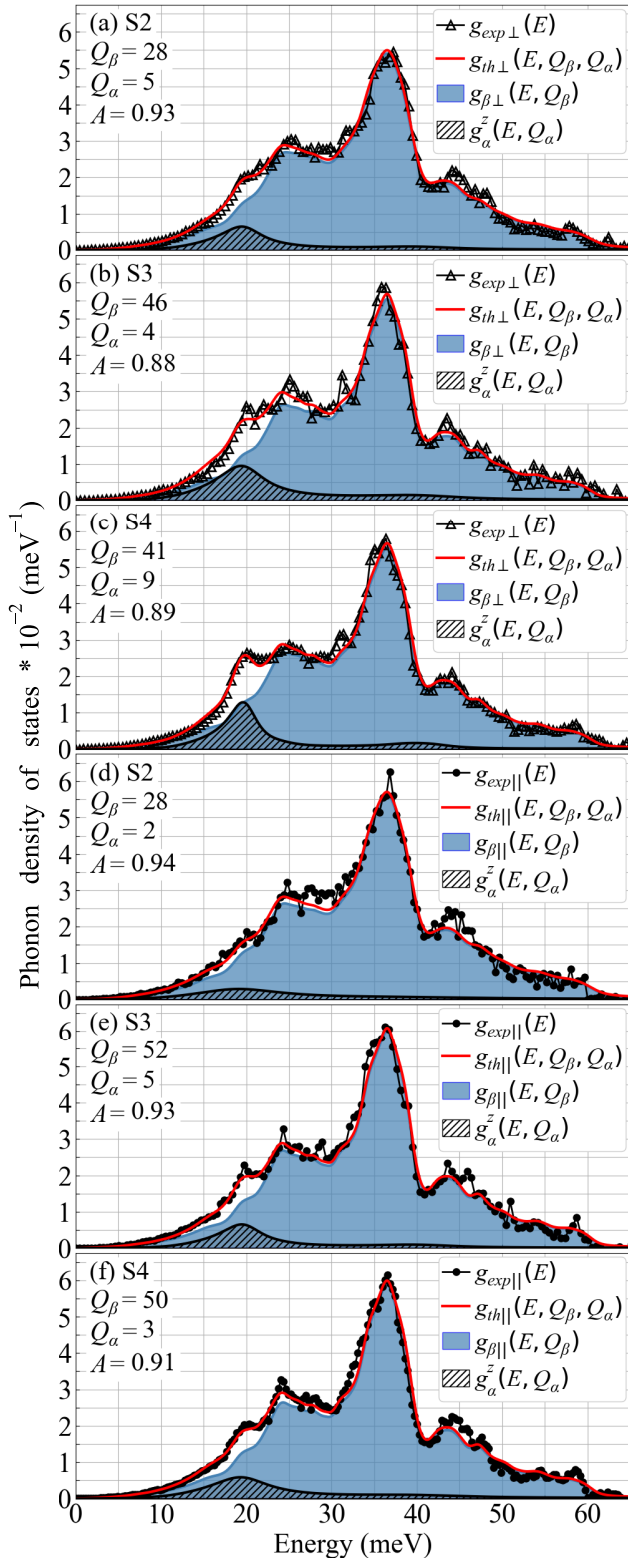


FIG. 8. Fe-partial PDOS of S2–S4 obtained at room temperature with the x-ray wave vector oriented perpendicular [(a)–(c)] and parallel [(d)–(f)] to the nanorods. The experimental spectra (symbols) are compared with the results of the least-squares fit (solid red line), decomposed into the weighted contributions of the direction-projected $\beta\text{-FeSi}_2$ and the z -polarized $\alpha\text{-FeSi}_2$ PDOS. The quality factors Q_β and Q_α are given together with the relative $\beta\text{-FeSi}_2$ contribution A .

the well studied epitaxial relation of $\beta\text{-FeSi}_2$ on the Si(111) surface also applies for Si(110) as depicted in Fig. 6(a). As a consequence, the $\beta\text{-FeSi}_2$ nanorods grow endotaxially to form a coherent interface with the Si(111) plane. Therefore the height values given in Table I can be seen as a lower limit since the $\beta\text{-FeSi}_2$ crystal of the nanorods is partially embedded into the Si substrate.

Using these epitaxial relations, the relative contributions of x -, y -, and z -polarized phonons to the experimental PDOS can be calculated, as briefly discussed above and described in detail in [86]. For the spectra obtained along Si[$\bar{1}10$], the x-ray wave vector is either parallel to (i) $\beta\text{-FeSi}_2[010]$ or (ii) $\beta\text{-FeSi}_2[001]$. The projection along the three main crystallographic directions of the $\beta\text{-FeSi}_2$ crystal then leads to average contributions of $A_x = 0$, $A_y = A_z = 0.5$, i.e., a zero contribution of x -polarized phonons. Across the rods, with the x-ray wave vector aligned along Si[001], the corresponding crystal directions are (i) $\beta\text{-FeSi}_2[140]$ and (ii) $\beta\text{-FeSi}_2[104]$. This leads to average relative contributions of $A_x = 0.09$, $A_y = A_z = 0.455$. Accordingly, the specific epitaxial relation between the $\beta\text{-FeSi}_2$ unit cell and Si(110) surface in the case of the nanorods leads to a reduced contribution of x -polarized vibrations to the PDOS compared to the polycrystalline film and results in a reduction of states at 24–28 meV and an enhancement at 40–45 meV.

The additional peak at 20 meV observed in the experimental PDOS of the $\beta\text{-FeSi}_2$ nanorods, however, cannot be explained by these epitaxial relations. It has been reported previously, that interface- and surface-specific vibrational modes are mainly localized in the first few monolayers [39,87]. The relatively large size of the nanorods implies a low surface/interface-to-volume ratio and consequently a significant contribution of surface or interface specific modes to the overall PDOS is not expected. In addition, the $\beta\text{-FeSi}_2(100)$ surface PDOS depicted in Fig. 6(c), which would be predominant in the case of possible surface effects, exhibits a strong contribution between 12–18 meV while the experimental data shows no enhancement of states in this range. Since the peak intensity at 20 meV is increasing with increasing annealing time from S2 to S4, also remnants of the precursor $\alpha\text{-FeSi}_2$ nanowires can be excluded as an origin in the case of S3 and S4. The reason for the occurrence of additional states at 20 meV could be an interlayer of another Fe-Si phase at the $\beta\text{-FeSi}_2/\text{Si}$ interface. For the growth of $\beta\text{-FeSi}_2$ on Si surfaces it was experimentally observed [3] and theoretically described [77,88] that the interface energy between the two components, having a rather large lattice mismatch, can be reduced by an $\alpha\text{-FeSi}_2$ interlayer. Furthermore, the z -polarized PDOS of $\alpha\text{-FeSi}_2$ exhibits a distinct peak at 20 meV [86]. For other Fe-Si phases reported to form on Si surfaces, e.g., FeSi [89] or Fe_3Si [39], this is not the case. Moreover, a previous study on $\alpha\text{-FeSi}_2$ nanowires showed that the epitaxial relation of the $\alpha\text{-FeSi}_2$ crystal and the Si(110) surface leads to a zero contribution of z -polarized phonons along and a very small contribution across the nanowire orientation. In both cases, this could not explain the distinct increase of intensity at 20 meV observed for S3 and S4. A possible explanation for the phenomenon observed here is that the transformation of the nanowires into $\beta\text{-FeSi}_2$ is accompanied by the formation of an $\alpha\text{-FeSi}_2$ interlayer which exhibits another epitaxial

relation with the Si(110) surface than the precursor α -FeSi₂. This reorientation of the α -FeSi₂ on the Si(110) surface then could result in a more pronounced contribution of z -polarized α -FeSi₂ phonons.

Under this assumption, the experimental spectra were modeled by a combination of the direction-projected *ab initio* PDOS of β -FeSi₂, weighted by A_x , A_y , and A_z as discussed above, and the *ab initio* z -polarized PDOS of α -FeSi₂ [86]. Generally, the comparison of the nanorod PDOS with the *ab initio* calculations for bulk β -FeSi₂ shows a broadening of the experimental PDOS features which is larger than the experimental resolution. This is attributed to phonon scattering at lattice defects, which are predominantly located at interfaces and surfaces [39,86,90]. The damping of the experimental PDOS can be modeled by convolution of the *ab initio* calculated PDOS with the damped harmonic oscillator (DHO) function [91,92]. The DHO function introduces an energy-dependent broadening of the spectral features quantified by the quality factor Q , which is inversely proportional to the strength of the damping. Moreover, the different energy resolution of the NIS experiments of S2–S4 has to be accounted for in order to assure a correct comparison of the Q values. Therefore the *ab initio* PDOS is calculated from the absorption probability density of β -FeSi₂ which is convoluted with a Voigt function with the FWHM equal the energy resolution function of the respective sample. The model function $g_{th}(E)$ is defined as

$$g_{th}(E, Q_\beta, Q_\alpha) = A g_\beta(E, Q_\beta) + (1 - A) g_\alpha^z(E, Q_\alpha), \quad (1)$$

where A is the relative β -FeSi₂ contribution, g_β the direction-projected *ab initio* calculated PDOS of β -FeSi₂, g_α^z the *ab initio* calculated z -polarized PDOS of α -FeSi₂, and Q_β , Q_α the quality factors used for the DHO convolution of the respective PDOS. The model function was fitted to the experimental results obtained along and across the nanorods by the least-squares method with A , Q_β and Q_α as fit parameters. Similarly to S1, the energy scale of the *ab initio* β -FeSi₂ PDOS is scaled by a factor of 0.98 to compensate a small shift between theory and experiment.

The resulting curves and fit parameters are given in Fig. 8, where $g_{th}(E)$ is plotted with a solid red line together with the β -FeSi₂ (blue) and α -FeSi₂ (hatched) subspectra. For comparison, fitting of the PDOS of S1 with the *ab initio* β -FeSi₂ PDOS leads to $Q_\beta = 100$ for both directions. The damping of the main peak is well reproduced by the model function. Despite the very similar size of the nanorods, significantly lower Q_β values and consequently a stronger phonon damping is observed for S2 compared to S3 and S4. As evidenced by the RHEED and AFM studies, the transformation process of the α -FeSi₂ nanowires into β -FeSi₂ nanorods is not completed in the case of S2 and therefore a higher concentration of lattice defects, and consequently stronger phonon damping in the β -FeSi₂ crystal, can be expected. Furthermore, S2 was measured under UHV conditions as described above, while S3 and S4 were capped with 4 nm of Si. However, for endotaxial α -FeSi₂ nanowires with similar diameters a significant effect of the capping on the lattice dynamics was not observed [72]. The z -polarized PDOS of α -FeSi₂ shows a good agreement with the peak at 20 meV. The values of Q_α are very small compared to Q_β , indicating a significantly stronger damping

in the α -FeSi₂ interlayer compared to the larger β -FeSi₂ crystal. This is in agreement with the reports of an either strained or disordered α -FeSi₂ layer at the Si/ β -FeSi₂ interface [3,77]. In addition, the experimental spectra were fitted by replacing the z -polarized α -FeSi₂ PDOS with the direction-projected PDOS α -FeSi₂ nanowires on Si(110) [72]. In the case of S2, this leads to a similarly good agreement between experiment and theory and the same R-squared values as for the approach described above. Consequently, for S2, the additional states at 20 meV can at least partially be attributed to the contribution of the remnant precursor α -FeSi₂ nanowires observed by AFM.

C. Thermodynamic and elastic properties

The thermodynamic and elastic properties obtained [93,94] from the *ab initio* calculated PDOS of the bulk crystal and the β -FeSi₂(100) surface slab as well as the experimental data are given in Table II. For all samples, the low-energy part of the PDOS can be described by the Debye model as $g(E) = \alpha E^2$. The velocity of sound v_S can then be calculated from the factor α [95] and is also given in Table II. The corresponding fits were done for the energy range between 4 to 12 meV for the bulk *ab initio* and experimental PDOS, for the surface *ab initio* PDOS the range was set from 4.5 to 8.5 meV.

Due to their similar vibrational behavior, the y and z directions of the direction-projected *ab initio* PDOS are merged in Table II. The shift in energy observed in Figs. 6(b) and 6(c) for the x - and yz -polarized phonons is reflected in the thermoelastic properties of the β -FeSi₂ bulk crystal and the β -FeSi₂(100) surface slab, which show a softer vibrational behavior in all values along x direction compared to the yz plane. These differences are even more pronounced for the β -FeSi₂(100) surface because of the broken translational symmetry. For example, an increase of 57% of the out-of-plane mean squared displacement $\langle x^2 \rangle$ along x compared to the in-plane vibrations along yz is observed. The general lattice softening of the (100) surface compared to the bulk crystal is most prominently reflected in the reduction of v_S by 52%. The temperature-dependent values of S1 show only a slight increase of the mean force constant F as well as v_S at 11 K compared to room temperature, which indicates a harmonic crystal lattice. The confinement of the available phase space at 11 K reduces $\langle x^2 \rangle$ by less than half while the vibrational entropy S_V and lattice heat capacity C_V approach zero. For the nanorods of S2–S4 most of the values agree within the uncertainty with the room temperature results of S1. Furthermore, no systematic dependence on the measurement direction is observed.

The assumption of a perfect bulk lattice for the *ab initio* calculations leads to a stiffer crystal compared to the experimental values. In the polycrystalline film of S1, the atoms located at lattice imperfections and grain boundaries exhibit a lower coordination number compared to a perfect crystal lattice and consequently experience lower interatomic force constants. This is reflected by an increase of $\langle x^2 \rangle$ by 14% and a reduction of v_S by 10% compared to the *ab initio* values. Furthermore, the calculation of v_S from the slopes of the acoustic branches of the dispersion curves yield values of 5350 m/s along the x direction and 5874 m/s for the yz

TABLE II. Fe-partial mean force constant F , mean square displacement $\langle x^2 \rangle$, vibrational entropy S_V , and lattice heat capacity C_V , calculated from the experimental PDOS of S1–S4 obtained along the indicated Si surface directions (compare Fig. 4). The coefficient α derived from the low-energy part of the PDOS [$g(E) = \alpha E^2$] and the sound velocity v_S are also given.

		F (N/m)	$\langle x^2 \rangle$ (\AA^2)	S_V (k_B/atom)	C_V (k_B/atom)	α (10^{-5} meV^{-3})	v_S (m/s)
theory	bulk <i>total</i>	281	0.0079	2.47	2.56	1.83(3)	5654(84)
	bulk <i>x</i>	255	0.0085	2.59	2.60	1.94(3)	5545(104)
	bulk <i>yz</i>	294	0.0076	2.41	2.54	1.77(5)	5712(82)
	surface <i>total</i>	165	0.0293	3.59	2.74	6.48(20)	3709(143)
	surface <i>x</i>	148	0.0386	3.60	2.76	6.88(40)	3636(216)
	surface <i>yz</i>	174	0.0246	3.59	2.73	6.28(19)	3748(112)
	experiment	S1 [$11\bar{2}$] RT	269(5)	0.0087(20)	2.54(2)	2.57(2)	2.41(3)
S1 [$\bar{1}10$] RT		263(5)	0.0088(20)	2.57(2)	2.59(2)	2.40(3)	5161(71)
S1 [$\bar{1}10$] 120 K		268(5)	0.0048(20)	0.068(2)	1.39(2)	2.30(3)	5241(73)
S1 [$\bar{1}10$] 11 K		274(5)	0.0037(20)	0.001(2)	0.003(2)	1.97(8)	5521(166)
S2 [001] RT		272(5)	0.0089(20)	2.54(2)	2.57(2)	2.56(2)	5055(47)
S2 [$\bar{1}10$] RT		272(5)	0.0088(20)	2.52(2)	2.57(2)	2.53(4)	5074(71)
S3 [001] RT		272(5)	0.0090(20)	2.55(2)	2.57(2)	2.54(8)	5066(155)
S3 [$\bar{1}10$] RT		265(5)	0.0089(20)	2.55(2)	2.58(2)	2.62(8)	5016(147)
S4 [001] RT		261(5)	0.0091(20)	2.59(2)	2.58(2)	2.56(4)	5056(78)
S4 [$\bar{1}10$] RT		270(5)	0.0088(20)	2.54(2)	2.57(2)	2.41(5)	5153(102)

plane. On average, this leads to the same overall v_S value as for the *ab initio* calculated PDOS, but the direction-resolved values show significant differences. Also the values presented here are significantly smaller compared to the mean velocity of sound of $v_S = 6210$ m/s obtained by first-principles calculations in Ref. [96]. A comparison of the v_S values calculated from the experimental PDOS shows on average larger values for S1 compared to the nanorods of S2–S4. Furthermore, the values calculated from the PDOS obtained along and across the nanorod orientation agree within the errors. The polycrystalline nature of the film S1 implies approximately equal contributions of *x*-, *y*-, and *z*-polarized phonons to the average v_S . For the nanorods, the relative contribution of each polarization is determined by the specific orientation of the β -FeSi₂ unit cell on the Si(110) surface. Considering the epitaxial relations discussed above, this should lead to a larger contribution of *yz*-polarized phonons and therefore to a higher v_S in the nanorods compared to S1 and also higher values along the nanorod orientation than across. Both effects are not observed, indicating that the speed of sound in the investigated nanostructures is reduced compared to the bulk crystal values most likely due to the high density of crystal defects within the nanorods and at the interfaces.

IV. CONCLUSIONS

Within this study, two types of β -FeSi₂ nanostructures were prepared and investigated. Firstly, a film was grown via solid phase epitaxy on a Si(111) substrate. By RHEED and XRD measurements the crystal structure was determined to be polycrystalline β -FeSi₂, by AFM a thickness of 16.2 nm was measured. Secondly, β -FeSi₂ nanorods were obtained by annealing of high-aspect-ratio α -FeSi₂ nanowires grown on Si(110). AFM and RHEED measurements showed that annealing for 2 hours at a temperature of 750 °C leads to a partial transformation of the nanowires into nanorods. After 3 hours

annealing at this temperature the process is completed. The average height of the nanorods ranged between 9.5–12 nm, their width between 40–52 nm. By RHEED a specific epitaxial orientation of the β -FeSi₂ crystal on the Si(110) surface was evidenced. Furthermore, a comparative EXAFS study on the Fe *K*-edge confirmed that the nanorods exhibit the same crystal structure as the β -FeSi₂ film.

The lattice dynamics of the nanostructures was investigated by a combined nuclear inelastic scattering and *ab initio* approach. The Fe-partial PDOS of the film and the nanorods was obtained by measurement with the x-ray beam oriented along orthogonal directions of the respective Si surface. These results were compared with the *ab initio* calculations for the bulk β -FeSi₂ crystal and the β -FeSi₂(100) surface. In the case of the polycrystalline film, the various domain orientations on average lead to an isotropic PDOS along both measurement directions, which shows a very good agreement with the *ab initio* calculations of the bulk crystal. Comparison of the PDOS in the temperature range from room temperature to 11 K shows a slight shift to lower energies for higher temperatures due to the thermal expansion of the crystal. The PDOS of the nanorods exhibits distinctly different spectral features compared to the film. The observed differences in the relative intensity of the PDOS features is explained by the epitaxial orientation of the β -FeSi₂ crystal on the Si(110) surface, which leads to a lower contribution of *x*-polarized phonons. Furthermore, additional states occurring at 20 meV are attributed to the formation of an α -FeSi₂ interlayer at the β -FeSi₂/Si interface. Under this assumption, the experimental results were modeled by the *ab initio* calculated PDOS. The modeling revealed a significantly stronger damping of the phonons in the α -FeSi₂ interlayer compared to the β -FeSi₂ crystal of the nanorods. The thermodynamic and elastic properties show a well pronounced softening of the lattice in the case of the *ab initio* calculated PDOS of the β -FeSi₂(100) surface compared to the bulk crystal.

ACKNOWLEDGMENTS

S.S. acknowledges the financial support by the Helmholtz Association (VH-NG-625) and BMBF (05K16VK4). P.P. acknowledges support by the Narodowe Centrum Nauki (NCN, National Science Centre) under Project No. 2017/25/B/ST3/02586 and the access to ESRF financed by the Polish Ministry of Science and High Education, decision number: DIR/WK/2016/19. The European Synchrotron

Radiation Facility is acknowledged for beamtime provision at the Nuclear Resonance beamline ID18. We thank J.-P. Celse for technical assistance during the experiment at ID18. We acknowledge DESY (Hamburg, Germany), a member of the Helmholtz Association HGF, for the provision of experimental facilities. Parts of this research were carried out at the High Resolution Dynamics Beamline P01 at PETRA III. We thank C. Hagemeyer and F.-U. Dill for technical assistance during the experiment at P01.

- [1] S. P. Murarka, *Intermetallics* **3**, 173 (1995).
- [2] L. J. Chen, *JOM* **57**, 24 (2005).
- [3] I. Berbezier, J. Chevrier, and J. Derrien, *Surf. Sci.* **315**, 27 (1994).
- [4] U. Starke, W. Weiss, M. Kutschera, R. Bandorf, and K. Heinz, *J. Appl. Phys.* **91**, 6154 (2002).
- [5] N. E. Christensen, *Phys. Rev. B* **42**, 7148 (1990).
- [6] Z. Yang, K. P. Homewood, M. S. Finney, M. A. Harry, and K. J. Reeson, *J. Appl. Phys.* **78**, 1958 (1995).
- [7] H. Kakemoto, Y. Makita, S. Sakuragi, and T. Tsukamoto, *Jpn. J. Appl. Phys.* **38**, 5192 (1999).
- [8] H. Katsumata, Y. Makita, N. Kobayashi, H. Shibata, M. Hasegawa, I. Aksenov, S. Kimura, A. Obara, and S. Uekusa, *J. Appl. Phys.* **80**, 5955 (1996).
- [9] Q. Wan, T. H. Wang, and C. L. Lin, *Appl. Phys. Lett.* **82**, 3224 (2003).
- [10] C. Giannini, S. Lagomarsino, F. Scarinci, and P. Castrucci, *Phys. Rev. B* **45**, 8822 (1992).
- [11] D. Leong, M. Harry, K. Reeson, and K. Homewood, *Nature (London)* **387**, 686 (1997).
- [12] T. Suemasu, Y. Negishi, K. Takakura, F. Hasegawa, and T. Chikyow, *Appl. Phys. Lett.* **79**, 1804 (2001).
- [13] T. Suemasu, K. Takakura, C. Li, Y. Ozawa, Y. Kumagai, and F. Hasegawa, *Thin Solid Films* **461**, 209 (2004).
- [14] D. Chi, *Thin Solid Films* **537**, 1 (2013).
- [15] A. V. Shevlyagin, D. L. Goroshko, E. A. Chusovitin, K. N. Galkin, N. G. Galkin, and A. K. Gutakovskii, *Sci. Rep.* **5**, 14795 (2015).
- [16] A. V. Shevlyagin, D. L. Goroshko, E. A. Chusovitin, S. A. Balagan, S. A. Dotsenko, K. N. Galkin, N. G. Galkin, T. S. Shamirzaev, A. K. Gutakovskii, A. V. Latyshev, M. Iinuma, and Y. Terai, *J. Appl. Phys.* **121**, 113101 (2017).
- [17] Z. Liu, S. Wang, N. Otagawa, Y. Suzuki, M. Osamura, Y. Fukuzawa, T. Ootsuka, Y. Nakayama, H. Tanoue, and Y. Makita, *Sol. Energy Mater. Sol. Cells* **90**, 276 (2006).
- [18] Y. Okuhara, D. Yokoe, T. Kato, S. Suda, M. Takata, K. Noritake, and A. Sato, *Sol. Energy Mater. Sol. Cells* **161**, 240 (2017).
- [19] Y. Okuhara, T. Kuroyama, D. Yokoe, T. Kato, M. Takata, T. Tsutsui, and K. Noritake, *Sol. Energy Mater. Sol. Cells* **174**, 351 (2018).
- [20] R. M. Ware and D. J. McNeill, *Proc. IEE* **111**, 178 (1964).
- [21] M. I. Fedorov and G. N. Isachenko, *Jpn. J. Appl. Phys.* **54**, 07JA05 (2015).
- [22] A. Nozariasbmarz, A. Agarwal, Z. A. Coutant, M. J. Hall, J. Liu, R. Liu, A. Malhotra, P. Norouzzadeh, M. C. Öztürk, V. P. Ramesh, Y. Sargolzaeiaval, F. Suarez, and D. Vashae, *Jpn. J. Appl. Phys.* **56**, 05DA04 (2017).
- [23] A. Laila, M. Nanko, and M. Takeda, *Materials* **7**, 6304 (2014).
- [24] J. Tani and H. Kido, *Jpn. J. Appl. Phys.* **40**, 3236 (2001).
- [25] H. Chen, X. Zhao, T. Zhu, Y. Lu, H. Ni, E. Müller, and A. Mrotzek, *Intermetallics* **13**, 704 (2005).
- [26] X. Du, P. Qiu, J. Chai, T. Mao, P. Hu, J. Yang, Y.-Y. Sun, X. Shi, and L. Chen, *ACS Appl. Mater. Interfaces* **12**, 12901 (2020).
- [27] T. Taniguchi, S. Sakane, S. Aoki, R. Okuhata, T. Ishibe, K. Watanabe, T. Suzuki, T. Fujita, K. Sawano, and Y. Nakamura, *J. Electron. Mater.* **46**, 3235 (2017).
- [28] U. Ail, S. Gorsse, S. Perumal, M. Prakasam, A. Umarji, S. Vives, P. Bellanger, and R. Decourt, *J. Mater. Sci.* **50**, 6713 (2015).
- [29] K. Watanabe, T. Taniguchi, S. Sakane, S. Aoki, T. Suzuki, T. Fujita, and Y. Nakamura, *Jpn. J. Appl. Phys.* **56**, 05DC04 (2017).
- [30] C.-L. Hsin, Y.-T. Liu, and Y.-Y. Tsai, *Nanotechnology* **28**, 485702 (2017).
- [31] S. Liang, R. Islam, D. J. Smith, and P. A. Bennett, *J. Cryst. Growth* **295**, 166 (2006).
- [32] S. K. Tobler and P. A. Bennett, *J. Appl. Phys.* **118**, 125305 (2015).
- [33] Z.-Q. Zou, X. Li, X.-Y. Liu, K.-J. Shi, and X.-Q. Guo, *Appl. Surf. Sci.* **399**, 200 (2017).
- [34] Y. F. Liang, S. Shang, J. Wang, Y. Wang, F. Ye, J. Lin, G. L. Chen, and Z. K. Liu, *Intermetallics* **19**, 1374 (2011).
- [35] J.-I. Tani, M. Takahashi, and H. Kido, *Phys. B: Condens. Matter* **405**, 2200 (2010).
- [36] M. Walterfang, W. Keune, E. Schuster, A. T. Zayak, P. Entel, W. Sturhahn, T. S. Toellner, E. E. Alp, P. T. Jochym, and K. Parlinski, *Phys. Rev. B* **71**, 035309 (2005).
- [37] M. A. Strocio and M. Dutta, *Phonons in Nanostructures* (Cambridge University Press, 2001).
- [38] D. Bozyigit, N. Yazdani, M. Yarema, O. Yarema, W. M. M. Lin, S. Volk, K. Vuttivorakulchai, M. Luisier, F. Juranyi, and V. Wood, *Nature (London)* **531**, 618 (2016).
- [39] J. Kalt, M. Sternik, I. Sergueev, J. Herfort, B. Jenichen, H.-C. Wille, O. Sikora, P. Piekarz, K. Parlinski, T. Baumbach, and S. Stankov, *Phys. Rev. B* **98**, 121409(R) (2018).
- [40] O. Sikora, J. Kalt, M. Sternik, A. Ptok, P. T. Jochym, J. Łażewski, K. Parlinski, P. Piekarz, I. Sergueev, H.-C. Wille, J. Herfort, B. Jenichen, T. Baumbach, and S. Stankov, *Phys. Rev. B* **99**, 134303 (2019).
- [41] S. Stankov, Y. Z. Yue, M. Miglierini, B. Sepiol, I. Sergueev, A. I. Chumakov, L. Hu, P. Svec, and R. Rüffer, *Phys. Rev. Lett.* **100**, 235503 (2008).
- [42] A. Seiler, P. Piekarz, S. Ibrahimkuty, D. G. Merkel, O. Waller, R. Pradip, A. I. Chumakov, R. Rüffer, T. Baumbach, K.

- Parlinski, M. Fiederle, and S. Stankov, *Phys. Rev. Lett.* **117**, 276101 (2016).
- [43] N. Driza, S. Blanco-Canosa, M. Bakr, S. Soltan, M. Khalid, L. Mustafa, K. Kawashima, G. Christiani, H.-U. Habermeyer, G. Khaliullin, C. Ulrich, M. Le Tacon, and B. Keimer, *Nat. Mater.* **11**, 675 (2012).
- [44] R. Pradip, P. Piekarz, D. G. Merkel, J. Kalt, O. Waller, A. I. Chumakov, R. Ruffer, A. M. Oleś, K. Parlinski, T. Baumbach, and S. Stankov, *Nanoscale* **11**, 10968 (2019).
- [45] K. Houben, J. K. Jochum, S. Couet, E. Menéndez, T. Picot, M. Y. Hu, J. Y. Zhao, E. E. Alp, A. Vantomme, K. Temst, and M. J. Van Bael, *Sci. Rep.* **10**, 5729 (2020).
- [46] S. Stankov, D. G. Merkel, J. Kalt, J. Göttlicher, J. Łazewski, M. Sternik, P. T. Jochym, P. Piekarz, T. Baumbach, A. I. Chumakov, and R. Ruffer, *Nanoscale Adv.* **4**, 19 (2022).
- [47] M. Seto, Y. Yoda, S. Kikuta, X. W. Zhang, and M. Ando, *Phys. Rev. Lett.* **74**, 3828 (1995).
- [48] W. Sturhahn, T. S. Toellner, E. E. Alp, X. Zhang, M. Ando, Y. Yoda, S. Kikuta, M. Seto, C. W. Kimball, and B. Dabrowski, *Phys. Rev. Lett.* **74**, 3832 (1995).
- [49] R. Ruffer and A. I. Chumakov, *Hyperfine Interact.* **128**, 255 (2000).
- [50] S. Stankov, R. Röhlberger, T. Slezak, M. Sladeczek, B. Sepiol, G. Vogl, A. I. Chumakov, R. Ruffer, N. Spiridis, J. Lazewski, K. Parlinski, and J. Korecki, *Phys. Rev. Lett.* **99**, 185501 (2007).
- [51] F. Scarinci, S. Lagomarsino, C. Giannini, G. Savelli, P. Castrucci, A. Rodia, and L. Scopa, *Appl. Surf. Sci.* **56-58**, 444 (1992).
- [52] D. Miquita, R. Paniago, W. Rodrigues, M. Moreira, H.-D. Pfannes, and A. de Oliveira, *Thin Solid Films* **493**, 30 (2005).
- [53] B. Krause, S. Darma, M. Kaufholz, H.-H. Gräfe, S. Ulrich, M. Mantilla, R. Weigel, S. Rembold, and T. Baumbach, *J. Synchrotron Radiat.* **19**, 216 (2012).
- [54] B. Ravel and M. Newville, *J. Synchrotron Radiat.* **12**, 537 (2005).
- [55] V. G. Kohn and A. I. Chumakov, *Hyperfine Interact.* **125**, 205 (2000).
- [56] H.-C. Wille, H. Franz, R. Röhlberger, W. A. Caliebe, and F.-U. Dill, *J. Phys.: Conf. Ser.* **217**, 012008 (2010).
- [57] R. Ruffer and A. I. Chumakov, *Hyperfine Interact.* **97-98**, 589 (1996).
- [58] S. Ibrahimkuty, A. Seiler, T. Prüßmann, T. Vitova, R. Pradip, O. Bauder, P. Wochner, A. Plech, T. Baumbach, and S. Stankov, *J. Synchrotron Radiat.* **22**, 91 (2015).
- [59] G. Kresse and J. Furthmüller, *Phys. Rev. B* **54**, 11169 (1996).
- [60] G. Kresse and J. Furthmüller, *Comput. Mater. Sci.* **6**, 15 (1996).
- [61] J. P. Perdew, K. Burke, and M. Ernzerhof, *Phys. Rev. Lett.* **77**, 3865 (1996).
- [62] R. Elmer, M. Berg, L. Carlen, B. Jakobsson, B. Noren, A. Oskarsson, G. Ericsson, J. Julien, T. F. Thorsteinsen, M. Guttormsen, G. Lovhoiden, V. Bellini, E. Grosse, C. Muntz, P. Senger, and L. Westerberg, *Phys. Rev. Lett.* **78**, 1396(E) (1997).
- [63] P. E. Blöchl, *Phys. Rev. B* **50**, 17953 (1994).
- [64] G. Kresse and D. Joubert, *Phys. Rev. B* **59**, 1758 (1999).
- [65] H. J. Monkhorst and J. D. Pack, *Phys. Rev. B* **13**, 5188 (1976).
- [66] K. Parlinski, Z. Q. Li, and Y. Kawazoe, *Phys. Rev. Lett.* **78**, 4063 (1997).
- [67] K. Parlinski, Software PHONON, version 6.15, Cracow, Poland (2015).
- [68] J. Chevrier, V. Le Thanh, S. Nitsche, and J. Derrien, *Appl. Surf. Sci.* **56-58**, 438 (1992).
- [69] A. N. Hattori, K. Hattori, and H. Daimon, *J. Phys.: Conf. Ser.* **61**, 404 (2007).
- [70] S. Oyarzún, A. K. Nandy, F. Rortais, J.-C. Rojas-Sánchez, M.-T. Dau, P. Noël, P. Laczkowski, S. Pouget, H. Okuno, L. Vila, C. Vergnaud, C. Beigné, A. Marty, J.-P. Attané, S. Gambarelli, J.-M. George, H. Jaffrès, S. Blügel, and M. Jamet, *Nat. Commun.* **7**, 13857 (2016).
- [71] Y. Yamamoto, *Surf. Sci.* **313**, 155 (1994).
- [72] J. Kalt, M. Sternik, B. Krause, I. Sergueev, M. Mikolasek, D. Merkel, D. Bessas, O. Sikora, T. Vitova, J. Göttlicher, R. Steininger, P. T. Jochym, A. Ptok, O. Leupold, H.-C. Wille, A. I. Chumakov, P. Piekarz, K. Parlinski, T. Baumbach, and S. Stankov, *Phys. Rev. B* **102**, 195414 (2020).
- [73] D. Das, J. C. Mahato, B. Bisi, B. Satpati, and B. N. Dev, *Appl. Phys. Lett.* **105**, 191606 (2014).
- [74] W. Lianwei, S. Qinwo, C. Xiangdong, L. Xian, L. Chenglu, and Z. Shichang, *Chin. Phys. Lett.* **12**, 301 (1995).
- [75] J. C. Mahato, D. Das, N. Banu, B. Satpati, and B. N. Dev, *Nanotechnology* **28**, 425603 (2017).
- [76] Z.-Q. Zou, W.-C. Li, J.-M. Liang, and D. Wang, *Acta Mater.* **59**, 7473 (2011).
- [77] L. Dobysheva, *Scr. Mater.* **133**, 37 (2017).
- [78] A. I. Chumakov, R. Ruffer, A. Q. R. Baron, H. Grünsteudel, H. F. Grünsteudel, and V. G. Kohn, *Phys. Rev. B* **56**, 10758 (1997).
- [79] V. G. Kohn, A. I. Chumakov, and R. Ruffer, *Phys. Rev. B* **58**, 8437 (1998).
- [80] N. Jedrecy, Y. Zheng, A. Waldhauer, M. Sauvage-Simkin, and R. Pinchaux, *Phys. Rev. B* **48**, 8801 (1993).
- [81] W. Raunau, H. Niehus, T. Schilling, and G. Comsa, *Surf. Sci.* **286**, 203 (1993).
- [82] J. E. Mahan, V. Le Thanh, J. Chevrier, I. Berbezier, J. Derrien, and R. G. Long, *J. Appl. Phys.* **74**, 1747 (1993).
- [83] T. Kimura, K. Akiyama, T. Watanabe, K. Saito, and H. Funakubo, *Jpn. J. Appl. Phys.* **42**, 4943 (2003).
- [84] Z. He, D. J. Smith, and P. A. Bennett, *Phys. Rev. Lett.* **93**, 256102 (2004).
- [85] J. Wu and S. Shimizu, *J. Appl. Phys.* **80**, 559 (1996).
- [86] J. Kalt, M. Sternik, B. Krause, I. Sergueev, M. Mikolasek, D. Bessas, O. Sikora, T. Vitova, J. Göttlicher, R. Steininger, P. T. Jochym, A. Ptok, O. Leupold, H.-C. Wille, A. I. Chumakov, P. Piekarz, K. Parlinski, T. Baumbach, and S. Stankov, *Phys. Rev. B* **101**, 165406 (2020).
- [87] T. Ślęzak, J. Lazewski, S. Stankov, K. Parlinski, R. Reitingner, M. Rennhofer, R. Ruffer, B. Sepiol, M. Slezak, N. Spiridis, M. Zajac, A. I. Chumakov, and J. Korecki, *Phys. Rev. Lett.* **99**, 066103 (2007).
- [88] M. A. Visotin, I. A. Tarasov, A. S. Fedorov, S. N. Varnakov, and S. G. Ovchinnikov, *Acta Crystallogr. Sect. B* **76**, 469 (2020).
- [89] P. P. Parshin, A. I. Chumakov, P. A. Alekseev, K. S. Nemkovski, J. Perßon, L. Dubrovinsky, A. Kantor, and R. Ruffer, *Phys. Rev. B* **93**, 081102(R) (2016).
- [90] B. Fultz, *Prog. Mater. Sci.* **55**, 247 (2010).
- [91] B. Fäk and B. Dorner, Technical Report No. 92FA008S, Tech. Rep. (Institute Laue Langevin, 1992) (unpublished).
- [92] B. Fäk and B. Dorner, *Phys. B: Condens. Matter* **234-236**, 1107 (1997).

- [93] A. I. Chumakov and W. Sturhahn, [Hyperfine Interact.](#) **123/124**, 781 (1999).
- [94] M. Y. Hu, T. S. Toellner, N. Dauphas, E. E. Alp, and J. Zhao, [Phys. Rev. B](#) **87**, 064301 (2013).
- [95] M. Y. Hu, W. Sturhahn, T. S. Toellner, P. D. Mannheim, D. E. Brown, J. Zhao, and E. E. Alp, [Phys. Rev. B](#) **67**, 094304 (2003).
- [96] J. Wu, X. Chong, Y. Jiang, and J. Feng, [J. Alloys Compd.](#) **693**, 859 (2017).